

PC-SwinMorph: Patch Representation for Unsupervised Medical Image Registration and Segmentation

Lihao Liu¹, Zhening Huang¹,
Pietro Liò¹, Carola-Bibiane Schönlieb¹, and Angelica I. Aviles-Rivero¹

University of Cambridge

Abstract. Medical image registration and segmentation are critical tasks for several clinical procedures. Manual realisation of those tasks is time-consuming and the quality is highly dependent on the level of expertise of the physician. To mitigate that laborious task, automatic tools have been developed where the majority of solutions are supervised techniques. However, in medical domain, the strong assumption of having a well-representative ground truth is far from being realistic. To overcome this challenge, unsupervised techniques have been investigated. However, they are still limited in performance and they fail to produce plausible results. In this work, we propose a novel unified unsupervised framework for image registration and segmentation that we called PC-SwinMorph. The core of our framework is two patch-based strategies, where we demonstrate that patch representation is key for performance gain. We first introduce a patch-based contrastive strategy that enforces locality conditions and richer feature representation. Secondly, we utilise a 3D window/shifted-window multi-head self-attention module as a patch stitching strategy to eliminate artifacts from the patch splitting. We demonstrate, through a set of numerical and visual results, that our technique outperforms current state-of-the-art unsupervised techniques.

1 Introduction

Image registration is a fundamental task in medical image analysis, which aims at finding a mapping that aligns an unaligned image to a reference one. The estimated spatial mapping (deformation field) seeks to best align the anatomical structure of interest. Image registration is relevant for several tasks in clinical practice including image-guided surgery [1,7], segmentation [6,15] and image reconstruction [13]. The outcome of those tasks greatly depends on the quality and efficiency of the registration technique. Although traditional image registration techniques [19,22,3,8] are able to generate a good mapping between images, they build upon costly optimisation schemes, which limits their efficiency when using a large volume of data. With that limitation in mind, several deep learning techniques have been proposed for registration.

A major category of approaches is supervised image registration techniques, where a good quality ground-truth is required for training e.g., [24,21,18,4,5]. However and unlike other tasks in image analysis, it is very difficult to obtain high quality ground-truth deformation fields or segmentation masks. Although a good mapping can be obtained from traditional methods or using synthetic data, this drawback hinders the performance and feasibility of those techniques in clinical practice.

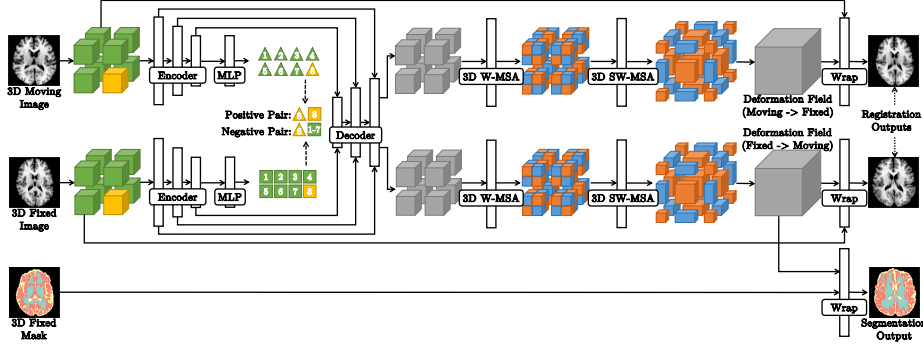


Fig. 1. The schematic illustration of the proposed PC-SwinMorph framework.

To mitigate the aforementioned strong requirement of supervised methods, a body of literature has been devoted to developing unsupervised techniques [17,14,12,25]. Those techniques have proposed different network mechanisms and explicit regularisers embedded in the architectures to enforce better correspondences between images. Although they have reported improved performance for unsupervised image registration, it is still limited. This is due to the lack of high-quality prior knowledge that introduces challenges such as failure in long-range correspondences. Motivated by this, we argue that we can extract better quality prior knowledge when we focus on a small patch. Medical images have complex image content due to the anatomical structures, which makes it hard to capture the image-to-image mapping. Hence, we hypothesize that patch embedding is a more meaningful representation for performance gain in medical data.

In this work, we proposed a unified framework for unsupervised image registration and segmentation, which we call PC-SwinMorph (**P**atch **C**ontrastive Strategy with **S**hifted-**w**indow multi-head self-attention based on **V**oxel**M**orph). The core of our framework is two patch-based strategies: patchwise contrastive registration and patching stitching with shifted-window multi-head self-attention. **Our contributions are as follows:** 1) We propose a patch-based framework for unsupervised image registration and segmentation, in which we highlight a patch-based contrastive strategy for enforcing a better fine detailed alignment and richer feature representation. 2) We design a patch stitching strategy to alleviate the splitting effect, caused by the patch representation, using 3D window/shifted-window multi-head self-attention module (3D W-MSA and 3D SW-MSA). 3) We evaluate our framework using two major medical benchmark datasets CANDI and LPBA40. We demonstrate from the numerical and visual results that our two patch-based strategies lead to better performance than the state-of-the-art techniques for unsupervised registration and segmentation.

2 Methodology

In this section, we first introduce the overall workflow. Then, we detail two core parts of our framework: i) a patchwise contrastive learning strategy, and ii) a patch based stitching strategy using shifted-window multi-head self-attention module.

2.1 Preliminaries & Workflow Overview Let x and y denote the moving (unaligned) and fixed (reference) 3D images respectively, where $x, y \in \mathbb{Z}^{w \times h \times d}$. We refer

to w, h, d as the width, height, depth of the 3D images, where $\mathbb{Z}^{w \times h \times d} \subset \mathbb{Z}^3$. We also denote the deformation field from x to y as $z_{x \rightarrow y}$, where $z_{x \rightarrow y} \in \mathbb{Z}^{w \times h \times d \times 3}$. The deformation fields for 3D images are in a 4 dimensional space, i.e., $\mathbb{Z}^{w \times h \times d \times 3} \subset \mathbb{Z}^4$. The four dimensions refer to each channel containing the pixel moving information in the w, h, d axis, respectively. Moreover, the deformation field $z_{x \rightarrow y}$ is parametrised with a spatial transformation function denoted as $\psi_{z_{x \rightarrow y}}$, such that, the registered results $x \circ \psi_{z_{x \rightarrow y}}$ is aligned with fixed image y .

The workflow of our PC-SwinMorph framework is displayed in Figure 1, which unifies unsupervised registration and segmentation tasks. Our framework uses an encoder to extract the CNN feature maps from the two given 3D images x and y . We then seek to estimate two deformation fields $z_{x \rightarrow y}$ and $z_{y \rightarrow x}$ from the extracted CNN feature maps with skip connections. After we obtain the deformation fields, we perform registration by using a spatial transformer[10] to warp the moving image x and the deformation field $z_{x \rightarrow y}$. We can then obtain the registration output ($x \circ \psi_{z_{x \rightarrow y}}$), where \circ denotes the wrap operation. Similarly, we can also use a spatial transformer to wrap the fixed image y and the deformation field $z_{y \rightarrow x}$ to obtain $y \circ \psi_{z_{y \rightarrow x}}$.

After registration, we also use the spatial transformer to wrap deformation field $z_{y \rightarrow x}$ and the segmentation mask of the image y . By doing this, we can obtain the segmentation mask for any image x . We underline that no masks are used in the training registration process, and they are only used in the testing segmentation stage. Therefore, our framework is a unified unsupervised registration and segmentation network.

2.2 Patch-based Strategy I: Patchwise Contrastive Registration The core of our technique is a patchwise strategy, which enforces an efficient and accurate registration:

Patch Generation. We first generate patches from the two 3D images instead of feeding directly the moving image x and the fixed image y as input. To do this, we evenly partition the 3D images into n^3 patches, that is, n pieces along the w, h, d axis without overlapping. We denote the generated patches from the moving and fixed images as p_i^x and p_i^y , where $i \in [1, n]$ and p_i^x and $p_i^y \in \mathbb{Z}^{\frac{w}{n} \times \frac{h}{n} \times \frac{d}{n}}$. For example, as shown in the Figure 1, we set n as 2. Therefore, both moving images and fixed images are split into 2^3 patches (8 patches).

Patchwise Registration. We first select a patch pair from the moving and fixed partitioned images at the same position (p_i^x and p_i^y). We then feed them into a two-symmetric weight-shared 3D encoder to extract the highly semantic CNN feature maps (see the two encoders in Figure 1). We use a single decoder to integrate all the CNN feature maps generated by the two encoders. Specifically, we recursively combine the CNN feature maps from high-to-low level (low-to-high image resolutions) to reconstruct two deformation field patches ($p_i^{z_{x \rightarrow y}}$ and $p_i^{z_{y \rightarrow x}}$) that have the same resolution as the input patches (p_i^x and p_i^y). See the decoder part in Figure 1. We repeat this process until every same-position patch pair has been fed through the encoder-decoder architecture to produce their corresponding two deformation field patches.

After obtaining the patchwise deformation fields, we stitch them to produce the full deformation field ($\hat{z}_{x \rightarrow y}$ and $\hat{z}_{y \rightarrow x}$). To achieve this, we use a 3D Swin Transformer Block [16]. See the 3D W-MSA and 3D SW-MSA module in Figure 1. We then use a spatial transformer to warp the moving image x and the stitched deformation field $\hat{z}_{x \rightarrow y}$ to obtain the composition $x \circ \psi_{\hat{z}_{x \rightarrow y}}$, and do the inverse registration from y to x .

As part of our unified framework, we can now use the estimated deformation field to do segmentation tasks. More precisely, in the testing stage, we use a spatial transformer, to warp the segmentation mask of the fixed image y_{seg} and (stitched) deformation field $\hat{z}_{y \rightarrow x}$, to generate the segmentation result $(y_{seg} \circ \psi_{\hat{z}_{y \rightarrow x}})$.

Reconstruction & Regularisation Terms. During the training process, we use two losses to guarantee a robust registration process. We first use a reconstruction loss, which enforces a plausible mapping to get the registered results as closest as possible to the template images. In our work, we use a normalised local cross-correlation loss (NCC loss) as the reconstruction loss. We denote the two input images as x and y . Then the local mean of x and y at pixel p are denoted as $\bar{x}(p)$ and $\bar{y}(p)$, respectively. The NCC loss is given as follow:

$$\mathcal{L}_{ncc}(x, y) = \sum_{p \in \Omega} \frac{\sum_{p_i} (x(p_i) - \bar{x}(p)) \cdot (y(p_i) - \bar{y}(p))}{\sqrt{\sum_{p_i} (x(p_i) - \bar{x}(p))^2 \cdot \sum_{p_i} (y(p_i) - \bar{y}(p))^2}}, \quad (1)$$

where the local mean $\bar{x}(p)$ and $\bar{y}(p)$ are calculated over a local window centered at pixel p with window length of 9, and in the domain $\Omega \subset \mathbb{Z}^{w \times h \times d}$. Our reconstruction loss reads:

$$\mathcal{L}_{recon} = \mathcal{L}_{ncc}(x \circ \psi_{\hat{z}_{x \rightarrow y}}, y) + \mathcal{L}_{ncc}(y \circ \psi_{\hat{z}_{y \rightarrow x}}, x). \quad (2)$$

We also include an L2 diffusion regulariser on the spatial gradients to obtain a smooth deformation field. It is given by:

$$\mathcal{L}_{smooth} = \sum_{p \in \Omega} \|\nabla \psi_{\hat{z}_{y \rightarrow x}}\|^2 + \sum_{p \in \Omega} \|\nabla \psi_{\hat{z}_{x \rightarrow y}}\|^2. \quad (3)$$

Patchwise Contrastive Loss. In representation learning, contrastive learning has been a successful perspective to learn distinctiveness. The main idea of contrastive learning is to maximise the similarity between images and their augmented views, whilst minimising the similarity between images from different groups. In contrast to existing contrastive methods, which select the positive and negative pairs between images in the dataset, we proposed to select the positive and negative pairs within the image internally. More precisely, after we recursively fed the moving and fixed patches p_i^x and p_i^y into the CNN encoders, we can obtain a set of high-level semantic CNN features maps for each patch. We use two linear projection layers (see the MLP in Figure 1) to map the high-level CNN semantic feature maps, for the moving and fixed patches, to a latent space, separately. Hence, the projected features are a calculated representation of the moving patch and fixed patch. We denote the projected features as f_i^x and f_i^y for the moving and fixed patch respectively, see the triangles and squares tagged as 1 to 8 in Figure 1. Between the two sets of projected features, we consider as a positive pair any part from the same partition position (f_i^x and f_i^y), otherwise a negative pair (f_i^x and f_j^y , where $i \neq j$). We then consider the following contrastive loss from f_i^x to f_i^y

$$\mathcal{L}_{contrast}^i(f_i^x, f_i^y) = -\log \frac{\exp(\text{sim}(f_i^x, f_i^y)/\tau)}{\sum_{j=1}^n \exp(\text{sim}(f_i^x, f_j^y)/\tau)}, \quad (4)$$

where $\text{sim}(u, v) = \frac{u^T v}{\|u\| \cdot \|v\|}$ is the cosine similarity between u and v . Moreover, τ is a temperature hyperparameter set as 1, and n is the number of patches. Hence, the final

patchwise contrastive loss is calculated as a weighted sum of contrastive loss from f_i^x to f_i^y and contrastive loss from f_i^y to f_i^z :

$$\mathcal{L}_{contrast} = -\frac{1}{2n} \sum_{i=1}^n (\mathcal{L}_{contrast}^i(f_i^x, f_i^y) + \mathcal{L}_{contrast}^i(f_i^y, f_i^z)). \quad (5)$$

2.3 Patch-based Strategy II: Patches Stitching with Shifted-window Multi-head Self-attention. To alleviate the blurring effect from the patch stitching, we propose to stitch the patches with multi-head self-attention. Specifically and for computational efficiency, we use the improved 3D window/shifted-window multi-head self-attention (3D W-MSA and 3D SW-MSA) from Swin Transformer [16].

3D W-MSA. To align with the definition of Swin Transformer, we define each deformation field patch $p_i^{z_{x \rightarrow y}}$ as a window. Each window is further split evenly into $m \times m \times m$ small non-overlapping regions $r_{ij}^{z_{x \rightarrow y}}$ where $i \in n^3, j \in m^3$. The original MSA performs the computation directly on the regions of an image with a size of $w \times h \times d$. Whereas the W-MSA calculates region relations inside windows, which can largely save computation time.

3D SW-MSA. *One core disadvantage of 3D W-MSA is that it lacks information exchange between windows*, since all the computation is performed on regions within a window, which means that simply applying the 3D W-MSA on the deformation field patches is not enough for dealing with the stitching effect see Fig. A in the supplementary material. Hence, based on the 3D W-MSA outputs, we further use the 3D SW-MSA to enhance information change between windows for stitching effect alleviating. We follow the cyclic-shifting strategy and move the window along the diagonal direction by one region $(\frac{w/n}{m} \times \frac{d/n}{m} \times \frac{h/n}{m})$. By cyclic-shifting, the generated window goes from n^3 to $(n+1)^3$. As shown in Figure 1, after the 3D SW-MSA, the window number increase from 8 to 27. With the increase of windows, regions from different windows are mingled for calculation, which allows information exchanges to erase the stitching effect. After the two modules, we stitch the self-attended window to obtain the stitched deformation field. We underline that our stitching strategy is like a clip-on function to refine the deformation field without introducing an additional loss term. Whilst the detailed description of W-MSA and SW-MSA can be found in [16].

3 Experimental Results

In this section, we detail the set of experiments performed to evaluate our proposed unified unsupervised registration and segmentation framework.

3.1 Datasets Description. We evaluate our framework using two publicly available datasets: the Child and Adolescent Neuro Development Initiative (CANDI) dataset [11] and the LONI Probabilistic Brain Atlas (LPBA40) dataset [20].

CANDI Dataset. CANDI dataset is comprised of 103 T1-weighted MRI scans with anatomic segmentation labels. The volume size of the MRI scans ranges from $256 \times 256 \times 128$ to $256 \times 256 \times 158$ voxels with a uniform space of $0.9375 \times 0.9375 \times 1.5 \text{ mm}^3$. We followed the convention used in [23] to group the same components from left and right brains together, forming overall 16 anatomical regions. For computational efficiency, we crop the volume to $160 \times 160 \times 128$ around the centre of the brain, which is large enough to incorporate the whole brain region.

TASK	TECHNIQUE	C-WM	C-CX	L-V	L-WM	L-CX	T-P	CAU	PUT	PAL	3-V	4-V	B-S	HIPP	AMY	CSF	V-DC	AVG
Registration	<i>VoxelMorph</i>	0.777	0.829	0.791	0.682	0.815	0.849	0.795	0.804	0.734	0.644	0.733	0.881	0.654	0.659	0.611	0.790	0.753
	<i>SYMNet</i>	0.787	0.840	0.778	0.717	0.838	0.883	0.825	0.853	0.787	0.657	0.710	0.865	0.680	0.675	0.599	0.805	0.769
	<i>DeepTag</i>	0.770	0.847	0.792	0.755	0.885	0.870	0.823	0.830	0.753	0.680	0.725	0.892	0.710	0.679	0.545	0.804	0.773
	<i>CycleMorph</i>	0.806	0.859	0.809	0.733	0.860	0.848	0.811	0.828	0.748	0.663	0.757	0.891	0.685	0.652	0.614	0.791	0.772
	PC-SwinMorph	0.825	0.880	0.847	0.801	0.908	0.892	0.859	0.880	0.802	0.676	0.784	0.913	0.763	0.698	0.614	0.824	0.812
Segmentation	<i>VoxelMorph</i>	0.776	0.831	0.783	0.698	0.812	0.860	0.802	0.830	0.764	0.673	0.738	0.881	0.663	0.669	0.574	0.797	0.759
	<i>SYMNet</i>	0.729	0.781	0.767	0.790	0.769	0.726	0.780	0.803	0.758	0.764	0.771	0.764	0.777	0.664	0.771	0.760	0.760
	<i>DeepTag</i>	0.759	0.842	0.786	0.758	0.883	0.867	0.812	0.834	0.756	0.659	0.708	0.887	0.718	0.696	0.538	0.800	0.771
	<i>CycleMorph</i>	0.812	0.869	0.787	0.759	0.869	0.864	0.811	0.844	0.776	0.680	0.737	0.891	0.709	0.690	0.570	0.801	0.780
	PC-SwinMorph	0.834	0.885	0.847	0.806	0.912	0.888	0.855	0.878	0.802	0.681	0.786	0.915	0.781	0.718	0.610	0.823	0.817

Table 1. Numerical comparisons between PC-SwinMorph and SOTA techniques on CANDI dataset. The best performance is highlighted in **bold** font.

LPBA40 Dataset. LPBA40 dataset contains 40 T1-weight 3D brain volumes from 40 healthy humans. The size of 3D volumes is $181 \times 217 \times 108$ with a uniform space of $1 \times 1 \times 1 \text{ mm}^3$. The 3D brain volume was manually segmented to identify 56 structures. Similar to the CANDI dataset, we crop the data to $160 \times 192 \times 160$ around the centre of 3D volumes to reduce the size of the volume whilst preserving all the brain regions. All the 56 structures are grouped into seven large regions in order to display the segmentation results more intuitively [14].

3.2 Implementation Details. In this subsection, we detail our implementation.

Data Pre-processing. We normalise the volumes to have zero mean and unit variance. For the CANDI dataset, we follow the data splitting in [23] and select 20 volumes as test data, 1 volume as the reference image, and the rest as training data. For the LPBA40 dataset, we set the first volume as the reference image, the next 29 images as training images, and the last 10 images as testing images.

Training Scheme. In the training stage, all parameters of convolutional layers are initialised by following the initialisation protocol of [9]. Adam optimiser is used with the initial learning rate setting as 10^{-3} . The learning rate decays by 0.1 scale every 50 epochs and terminates after 200 epochs. The batch size for both datasets is 1. All models are run on an NVIDIA A100 GPU with 80G RAM, which takes around 6 hours to train the model on the CANDI dataset and around 4 hours on the LPBA40 dataset.

Testing Scheme. During testing, unsupervised segmentation is performed based on learned parameters. We first fed the trained network with the moving image x and fixed images y to obtain the deformation field $\hat{z}_{y \rightarrow x}$. We then used a spatial transform network [10] to wrap the segmentation mask of fixed image (y_{seg}) and the deformation field $\hat{z}_{y \rightarrow x}$ to obtain the segmentation results of moving image ($y_{seg} \circ \psi_{\hat{z}_{y \rightarrow x}}$). With one NVIDIA A100 GPU, our method can process around 3.2 brain images per second.

Evaluation Protocol. To make our results comparable to other SOTA methods, we use the *Dice* similarity coefficient to evaluate the segmentation and registration quality of our model, which measures the overlap between ground truth and predicted mask.

3.3 Comparison to the State-of-the-Art Techniques. We compared our technique with recent unsupervised brain segmentation methods, including VoxelMorph [2], DeepTag [25], SYMNet [17], CycleMorph [12]. In general, all methods are based on the fundamental architecture of VoxelMorph. For a fair comparison, all models use the same backbone, VoxelMorph, which has been fine-tuned to achieve optimal performance.

Numerical Comparison. Tables 1 summarise performance-wise, in terms of the *Dice* coefficient, the compared SOTA methods, and our PC-SwinMorph. The numbers

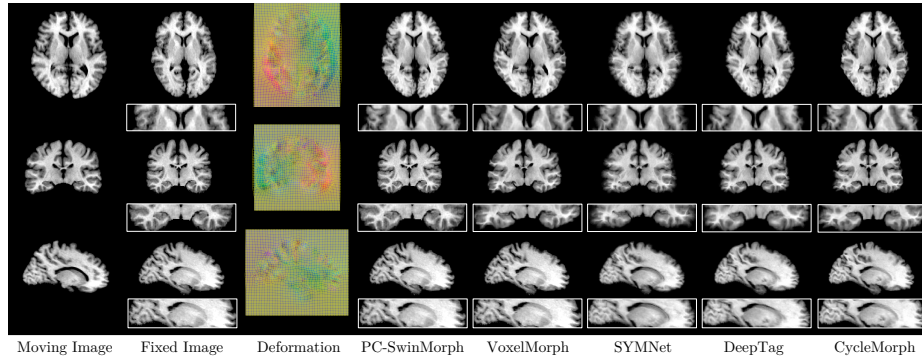


Fig. 2. Visual comparisons between PC-SwinMorph and other SOTA techniques for registration. The rows show the three views from 3D volumes. Zoom-in views highlight regions that shows improvements of our method in terms of preserving the global structures and fine local details.

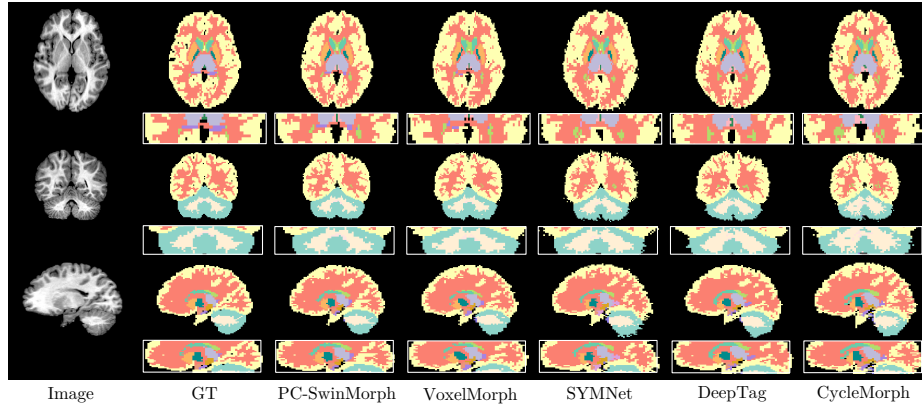


Fig. 3. Visual comparisons between PC-SwinMorph and other SOTA techniques for segmentation. Zoom-in views demonstrate that the proposed method preserved more details in different regions thus producing better segmentation results.

are obtained using the testing scheme described in section 3. In a closer look at the tables, we observe that for both data, our method outperforms all other SOTA methods with a large margin, including the overall performance as well as local performance on majority regions. Particularly, on the CANDI dataset our results report an improvement of 5.9% compared to VoxelMorph, and 3.9-4.3% against the other compared techniques. This performance gain is consistent on the LPBA40 dataset, where our method is 1.2-7.0% higher in performance than the SOTA methods; see Table A in supp. file.

Visual Comparison. We support the numerical results with additional visual results for our technique and the compared ones. Figure 3 shows some samples slices of the segmentation results predicted by VoxelMorph, SYMNet, DeepTag, CycleMorph, and our proposed method PC-SwinMorph. Whilst the results produced by the compared SOTA techniques are anatomically meaningful, they fail to capture fine details in several regions. By contrast, PC-SwinMorph is able not only to produce a better output but also capture details. The zoom-in views in Figure 3 highlights these effects. Overall, PC-SwinMorph can better accommodate with fine details of the brain structure, producing

segmentation closer to the ground truth. Figure 2 shows the wrapped images produced by different SOTA techniques as well as the proposed PC-SwinMorph. We can observe that our registration outputs are closer to the reference image, displaying fewer splitting effects from the patch generation whilst keeping fine details.

3.4 Ablation Study. We provide ablation results to further support the model design.

Contrastive Representation. A contrastive feature learning mechanism is embedded into the registration architecture which promotes feature-level learning. The contrastive loss forces the network to contrast the difference between the two extracted CNN feature maps and therefore, the network is more discriminative to different images via contrasting unaligned images and reference images. As shown in Table 2, *the testing results demonstrate this new mechanism significantly improve the segmentation performance by around 2-3% upon the baseline model.*

Patchwise Contrastive Learning.

Based on the idea of contrastive learning, we introduce a patchwise contrastive learning strategy. It uses a multilayer patch-based approach rather than operate on entire images. The Patchwise contrastive loss introduced in (5) encourages two corresponding patches, in the image, to map to a point in a learned feature space, at the same time drawing negative

if they match to other patches. This mechanism further boosts the registration performance and produces better segmentation results. From the *Dice* coefficient comparison reported in Table 2, we can observe that the patchwise contrastive approach offers an additional 2% improvement with respect to the contrastive learning approach. This improvement is observed in both the registration and segmentation performance. This introduced strategy offers an overall improvement of 4% when compared to the baseline.

The effect of 3D W-MSA & 3D SW-MSA. One of the main drawbacks of patchwise learning is the lack of information exchange between patches. The introduction of 3D W-MSA and 3D SW-MSA, which stitches the patches and enhances the performance across patches, has been demonstrated to be greatly effective. As shown in Table 2, the segmentation and registration performance on the CANDI dataset has been improved 2.65% and 3.06% respectively when using 3D SW-MSA. This performance behavior is prevalent on LPBA40 demonstrating consistent performance.

Our PC-SwinMorph	CANDI		LPBA40	
	Registration	Segmentation	Registration	Segmentation
Baseline (B)	0.753	0.759	0.720	0.728
B + PW	0.779	0.777	0.751	0.762
B + CL	0.771	0.772	0.760	0.766
B + PW + CL	0.791	0.792	0.779	0.783
B + PW + CL + SW	0.812	0.817	0.791	0.794

Table 2. Ablation Study. We denote the baseline as ‘B’, patchwise method as ‘PW’, contrastive loss as ‘CL’, and 3D SW-MSA as “SW”.

4 Conclusion

We introduce a novel unified unsupervised framework for image registration and segmentation. We propose to rethink these tasks from a patch-based perspective and introduce two patch-based strategies. Firstly, we introduce a novel patch-based contrastive strategy to obtain richer features and preserve anatomical details. Secondly, we design a patch stitching strategy to eliminate any inherent artifact from the patch-based partition. Our intuition behind the performance gain of our strategies is that through patches we capture not only global but also local spatial structures (more meaningful embeddings). We demonstrated that our technique reported SOTA performance for both tasks.

References

1. Aviles, A.I., Alsaleh, S.M., Hahn, J.K., Casals, A.: Towards retrieving force feedback in robotic-assisted surgery: A supervised neuro-recurrent-vision approach. *IEEE transactions on haptics* **10**(3), 431–443 (2016)
2. Balakrishnan, G., Zhao, A., Sabuncu, M.R., Guttag, J., Dalca, A.V.: Voxelmorph: a learning framework for deformable medical image registration. *IEEE transactions on medical imaging* **38**(8), 1788–1800 (2019)
3. Beg, M.F., Miller, M.I., Trounev, A., Younes, L.: Computing large deformation metric mappings via geodesic flows of diffeomorphisms. *International journal of computer vision* **61**(2), 139–157 (2005)
4. Cao, X., Yang, J., Zhang, J., Nie, D., Kim, M., Wang, Q., Shen, D.: Deformable image registration based on similarity-steered cnn regression. In: *International Conference on Medical Image Computing and Computer-Assisted Intervention*. pp. 300–308 (2017)
5. Cao, X., Yang, J., Zhang, J., Wang, Q., Yap, P.T., Shen, D.: Deformable image registration using a cue-aware deep regression network. *IEEE Transactions on Biomedical Engineering* **65**(9), 1900–1911 (2018)
6. Fu, Y., Liu, S., Li, H.H., Yang, D.: Automatic and hierarchical segmentation of the human skeleton in ct images. *Physics in Medicine & Biology* **62**(7), 2812 (2017)
7. Han, R., Uneri, A., Vijayan, R.C., Wu, P., Vagdargi, P., Sheth, N., Vogt, S., Kleinszig, G., Osgood, G., Siewerdsen, J.H.: Fracture reduction planning and guidance in orthopaedic trauma surgery via multi-body image registration. *Medical image analysis* **68**, 101917 (2021)
8. Hart, G.L., Zach, C., Niethammer, M.: An optimal control approach for deformable registration. In: *Conference on Computer Vision and Pattern Recognition*. pp. 9–16 (2009)
9. He, K., Zhang, X., Ren, S., Sun, J.: Delving deep into rectifiers: Surpassing human-level performance on imagenet classification (2015)
10. Jaderberg, M., Simonyan, K., Zisserman, A., Kavukcuoglu, K.: Spatial transformer networks (2016)
11. Kennedy, D.N., Haselgrove, C., Hodge, S.M., Rane, P.S., Makris, N., Frazier, J.A.: Candishare: a resource for pediatric neuroimaging data. *Neuroinformatics* **10**(3), 319–22 (2012 Jul 2012). <https://doi.org/10.1007/s12021-011-9133-y>
12. Kim, B., Kim, D.H., Park, S.H., Kim, J., Lee, J.G., Ye, J.C.: Cyclemorph: Cycle consistent unsupervised deformable image registration. *Medical Image Analysis* **71**, 102036 (2021)
13. Liu, J., Aviles-Rivero, A.I., Ji, H., Schönlieb, C.B.: Rethinking medical image reconstruction via shape prior, going deeper and faster: Deep joint indirect registration and reconstruction. *Medical Image Analysis* **68**, 101930 (2021)
14. Liu, L., Aviles-Rivero, A.I., Schönlieb, C.B.: Contrastive registration for unsupervised medical image segmentation. *arXiv preprint arXiv:2011.08894* (2020)
15. Liu, L., Hu, X., Zhu, L., Heng, P.A.: Probabilistic multilayer regularization network for unsupervised 3d brain image registration. In: *International Conference on Medical Image Computing and Computer-Assisted Intervention*. pp. 346–354. Springer (2019)
16. Liu, Z., Lin, Y., Cao, Y., Hu, H., Wei, Y., Zhang, Z., Lin, S., Guo, B.: Swin transformer: Hierarchical vision transformer using shifted windows. *arXiv preprint arXiv:2103.14030* (2021)
17. Mok, T.C., Chung, A.: Fast symmetric diffeomorphic image registration with convolutional neural networks. In: *IEEE/CVF conference on computer vision and pattern recognition*. pp. 4644–4653 (2020)
18. Rohé, M.M., Datar, M., Heimann, T., Sermesant, M., Pennec, X.: Svf-net: Learning deformable image registration using shape matching. In: *International conference on medical image computing and computer-assisted intervention*. pp. 266–274. Springer (2017)

19. Rueckert, D., Sonoda, L.I., Hayes, C., Hill, D.L., Leach, M.O., Hawkes, D.J.: Nonrigid registration using free-form deformations: application to breast mr images. *IEEE transactions on medical imaging* **18**(8), 712–721 (1999)
20. Shattuck, D.W., Mirza, M., Adisetiyo, V., Hojatkashani, C., Salamon, G., Narr, K.L., Poldrack, R.A., Bilder, R.M., Toga, A.W.: Construction of a 3D probabilistic atlas of human cortical structures. *NeuroImage* **39**(3), 1064–1080 (Feb 2008). <https://doi.org/10.1016/j.neuroimage.2007.09.031>, <http://linkinghub.elsevier.com/retrieve/pii/S1053811907008099>
21. Sokooti, H., De Vos, B., Berendsen, F., Lelieveldt, B.P., Išgum, I., Staring, M.: Nonrigid image registration using multi-scale 3d convolutional neural networks. In: *International conference on medical image computing and computer-assisted intervention*. pp. 232–239. Springer (2017)
22. Vercauteren, T., Pennec, X., Perchant, A., Ayache, N.: Diffeomorphic demons: Efficient non-parametric image registration. *NeuroImage* **45**(1), S61–S72 (2009)
23. Wang, S., Cao, S., Wei, D., Wang, R., Ma, K., Wang, L., Meng, D., Zheng, Y.: Lt-net: Label transfer by learning reversible voxel-wise correspondence for one-shot medical image segmentation (2020)
24. Yang, X., Kwitt, R., Styner, M., Niethammer, M.: Quicksilver: Fast predictive image registration—a deep learning approach. *NeuroImage* **158**, 378–396 (2017)
25. Ye, M., Kanski, M., Yang, D., Chang, Q., Yan, Z., Huang, Q., Axel, L., Metaxas, D.: Deeptag: An unsupervised deep learning method for motion tracking on cardiac tagging magnetic resonance images. In: *Proceedings of the IEEE/CVF Conference on Computer Vision and Pattern Recognition*. pp. 7261–7271 (2021)